A Theory for High-Throughput Genetic Interaction Screening

Madeline E. McCarthy[1], William B. Dodd[1], Xiaoming Lu[1], Nishi D. Patel[1], Charlotte V. Haskell[1], Hugo Sanabria[2], Mark A. Blenner[1,3], and Marc R. Birtwistle[1,4,#]

[1]Department of Chemical and Biomolecular Engineering, Clemson University
[2]Department of Physics and Astronomy, Clemson University
[3]Department of Chemical and Biomolecular Engineering, University of Delaware
[4]Department of Bioengineering, Clemson University
[#]Correspondence: mbirtwi@clemson.edu

Abstract

Systematic, genome-scale genetic screens have been instrumental for elucidating genotype-phenotype relationships, but approaches for probing genetic interactions have been limited to at most ~100 pre-selected gene combinations in mammalian cells. Here, we introduce a theory for high-throughput genetic interaction screens. The theory extends our recently developed Multiplexing using Spectral Imaging and Combinatorics (MuSIC) approach to propose ~10^5 spectrally unique, genetically-encoded MuSIC barcodes from 18 currently available fluorescent proteins. Simulation studies based on constraints imposed by spectral flow cytometry equipment suggest that genetic interaction screens at the human genome-scale may be possible if MuSIC barcodes can be paired to guide RNAs. While experimental testing of this theory awaits, it offers transformative potential for genetic perturbation technology and knowledge of genetic function. More broadly, the availability of a genome-scale spectral barcode library for non-destructive identification of single-cells could find more widespread applications such as traditional genetic screening and high-dimensional lineage tracing.

Introduction

Understanding which genes play essential roles in a cellular or organismal process is crucial to our understanding of biology[1]. This can be accomplished by perturbing genes and observing the corresponding phenotype alterations[2]. This process, when applied in parallel to multiple genes one-at-a-time, is known as genetic screening[3,45–8]. Historically, there have been several methods for performing genetic screens, including Zinc finger nucleases (ZFNs) and transcription activator-like effector nucleases (TALENs) which are engineered nucleases that induce DNA DSBs at specific locations[9,10], RNAi which uses double stranded RNAs (or a short hairpin (sh)RNA) to knock down the gene-of-interest[11], and CRISPR which induces DNA breaks or alters transcription at specific sites in the genome[12,13 15].

While these gene perturbation technologies have revolutionized biomedical science, most genome-scale screens (outside of organisms like *S. cerevisae*[16]) remain limited to one gene at a time[17]. However, often genes cooperate with one another to influence phenotype. Such cooperation is called genetic interaction[18–21]. Recent approaches have made progress towards larger scale genetic interaction screening. For example, cloning two different CRISPR gRNAs into a single plasmid enables interaction screening for ~100 pre-selected genes [19,25–27]. Other approaches include dual recombinase-mediated cassette exchange to create mosaic *in vivo* models harboring multiple desired cancer driver mutations[28], or using protein epitope combinatorial barcodes (pro-codes) with mass cytometry to perform high-dimensional CRISPR screens on 100s of selected genes in single cells[29]. The sheer number of observations that must be made to cover human gene interactions space almost necessitates a single-cell approach, like Perturb-seq[30–32]. However, genetic interaction screening approaches that scale past ~100 genes have yet to be described.

Here, we propose that our recently developed fluorescence **mu**ltiplexing with **s**pectral **i**maging and **c**ombinatorics (MuSIC)[33] approach may be compatible with single cell genetic interaction screening that could scale to the full human genome. MuSIC uses combinations of fluorophores (proteins or small molecules) to create spectrally unique MuSIC probes. Here we introduce the concept of further combining MuSIC probes into MuSIC barcodes for increased diversity and thus multiplexing. Moreover, because these spectral barcodes are fluorescence-based, they can be read non-destructively. Theory and simulations based on currently available fluorescent proteins suggests that given a palette of 18 fluorescent proteins, ~400,000 MuSIC

barcodes could be generated, far surpassing human genome-scale. Simulations suggest that given current spectral flow cytometry equipment and experimental noise, human genome-scale genetic interaction screens may be possible. More advanced instrument hardware such as more excitation lasers and/or higher resolution emission spectra could increase such capabilities. While experimental testing of this theory awaits, it offers transformative potential for genetic perturbation technology and knowledge of genetic function. More broadly, the availability of a genome-scale spectral library for non-destructive cell identification could find more widespread applications such as traditional genetic screens and high-dimensional lineage tracing.

Methods

Availability, Code Overview, and Simulation. All MATLAB code and raw data used for simulations are included in the supplementary code zip file associated with this manuscript. The scripts `GenerateProbeData_3l_HN.m`, `GenerateProbeData_3l_LN.m`, `GenerateProbeData_5l_HN.m`, and `GenerateProbeData_5l_LN.m` are used for generating the list of good probes for single probes, barcodes, and two barcodes, for 3 lasers/high noise (HN), 3 lasers/low noise (LN), 5 lasers/high noise, and 5 lasers/low noise respectively. The core of these scripts is done by the functions `RemoveProbes_onebyone.m`, `RemoveBarcodes_onebyone.m`, and `RemoveTwoBarcodes_onebyone.m`, respectively. The README file contains relevant information on the code for execution and reproducing the results. These simulations were performed in MATLAB using 40 CPUs on the Palmetto supercomputing cluster at Clemson University.

Data Sources. Emission spectra, excitation spectra, and brightness for fluorescent proteins were gathered from *fpbase.org* (**Supplementary Table 1** and references therein). Specifications for flow cytometer noise, excitation channels, and emission binning were obtained from the Aurora and Northern Lights flow cytometer user guides on *cytekbio.com*.

Simulated FRET Efficiency and MuSIC Probe Selection. FRET efficiency ε between two fluorophores is typically calculated as follows

$$\varepsilon = \frac{1}{1 + \left(\frac{r}{R_0}\right)^6} \quad (1)$$

where r is the distance between the two fluorophores and R_0 is the Förster radius[34]. The Förster radius is the distance between fluorophores that gives a 50% FRET efficiency[34]. Thus, to estimate the FRET efficiency between any given pair of fluorescent proteins, we must calculate R_0 and r.

The Förster radius can be cast as follows[35]

$$R_0 = [\beta * \mathrm{K}^2 * Q_D * e_A * J]^{\frac{1}{6}}\, nm \quad (2)$$

where β is a constant (which also converts to nm), K^2 is an orientation factor between the two fluorophores, Q_D is the donor quantum yield, e_A is the maximal acceptor extinction coefficient ($M^{-1*}cm^{-1}$), and J is the spectral overlap integral. The value of K^2 is not usually known (nor easily measurable) but is assumed to be a constant value of 2/3 for isotropic reorientation of the coupled fluorophores [36]. This value may not be 2/3 for fluorescent protein tandems but in practice, deviations can be accounted for by the constant β[37]. J is calculated as follows

$$J = \int F_D(\lambda) E_A(\lambda)\, \lambda^4 d\lambda \qquad (3)$$

where F_D is the normalized emission spectra of the donor and E_A is the normalized excitation spectra of the acceptor, which both are evaluated at wavelength λ. Here, the spectral data is normalized to have a maximum value of 1. We calculate the overlap integral using the function `trapz` in MATLAB (see code) with bounds from λ = 300 to 800 nm. The value for β is estimated to be $6.33*10^{-6}$ based on a known Förster radius of 6.1 nm for mTFP-Venus[38] (along with known Q_D, and e_A, and J calculated as above).

The closest physical distance that chromophores of fluorescent proteins can be is ~3 nm[39]. Furthermore, most high FRET producing pairs have an R_0 greater than 5 nm[40]. Thus, we do not consider MuSIC probes that have R_0 < 5 nm. Since the distance between fluorescent proteins can usually be adjusted (by linker length, for example), we set $r = R_0$ in simulations, giving a FRET efficiency of 50% for each MuSIC probe with more than one fluorescent protein.

Simulating Reference Emission Spectra for MuSIC probes. There are three classes of MuSIC probes that require separate consideration for simulating their emission spectra: those made of a (i) single fluorescent protein, (ii) two fluorescent proteins, and (iii) three fluorescent proteins. The below equations are used to generate columns of the reference matrix **R** (see below) for unmixing. Each simulated spectra for a single excitation channel has a value every nm from 300 to 800 nm. The below model assumes that tandem fluorescent proteins have the same properties as the monomers, that static quenching is not a dominant feature, and that fluorescent protein maturation is not a significant factor for the spectra. We assume cross-talk is negligible,

but for all intents and purposes, it would be observed as effective FRET-related activity and therefore is expected to not have additional functional consequences for simulation results. We also note here that this model does not take into account detector quantum efficiency. Avalanche Photodiode (APD) detectors (used in the Cytek instruments) generally have slightly lower quantum efficiency in the lower wavelengths (UV/Blue), but so long as all reference spectra and samples are measured with the same instrument, this would not introduce any further bias and not affect the conclusions drawn here.

To simulate the emission intensity spectra I for a single fluorescent protein MuSIC probe, given a particular excitation wavelength $(\lambda_{ex})$and vector of emission wavelengths from 300 to 800nm at every nm $(\boldsymbol{\lambda})$, the following equation is used (adapted from Schwartz et. al)[41]

$$I(\boldsymbol{\lambda}) = E(\lambda_{ex}) * C * B * F(\boldsymbol{\lambda}) \quad (4)$$

Where E is the fraction of excited fluorophores and is a function of excitation wavelength (explained below), C is the relative probe concentration (taken as 1 for reference spectra assuming a null condition of equal expression levels between probes), B is the brightness (product of maximal extinction coefficient and quantum yield), and F is the normalized emission spectra vector of the fluorescent protein (normalized as above). $E(\lambda_{ex})$ is given by the fluorescent protein's normalized excitation spectra at the designated excitation wavelength.

For MuSIC probes with two fluorescent proteins, called 1 and 2 ordered from blue to red, the emission intensity spectra $I(\boldsymbol{\lambda})$ has three contributing components: acceptor emission due to FRET ($I_{2,1}$), donor emission (I_1), and acceptor emission due to direct excitation (I_2). The overall emission intensity spectra I is the sum of the three components

$$I = I_{2,1} + I_1 + I_2 \quad (5)$$

Each of these terms depends on the FRET efficiency. We assume that FRET efficiency is reduced due to any direct acceptor (2) excitation, since excited acceptors would not be able to undergo FRET. This adjusted FRET efficiency, ε_{adj}, is calculated as follows

$$\varepsilon_{adj} = \varepsilon * \left(1 - E_2(\lambda_{ex})\right) \quad (6)$$

where E_2 is the fraction of excited fluorophores for fluorescent protein 2 and the term (1-E_2) denotes the fraction of fluorescent protein 2 molecules that have not been directly excited.

Fluorescent protein 2 emission due to FRET from fluorescent protein 1 is then calculated by

$$I_{2,1}(\boldsymbol{\lambda}) = E_1(\lambda_{ex}) * \varepsilon_{adj} * C * B_2 * F_2(\boldsymbol{\lambda}) \quad (7)$$

This emission intensity is proportional to emission properties of fluorescent protein 2 (emission spectra and brightness), the fraction of excited molecules for fluorescent protein 1, and the adjusted FRET efficiency between the two fluorescent proteins.

Fluorescent protein 1 emission is calculated by

$$I_1(\boldsymbol{\lambda}) = E_1(\lambda_{ex}) * (1 - \varepsilon_{adj}) * C * B_1 * F_1(\boldsymbol{\lambda}) \quad (8)$$

This emission is calculated similarly to that above for a single fluorescent protein; however, it is corrected to only take into account the fraction of excited molecules that are not undergoing FRET $(1 - \varepsilon_{adj})$.

Fluorescent protein 2 emission due to direct excitation is calculated by

$$I_2(\boldsymbol{\lambda}) = E_2(\lambda_{ex}) * \left(1 - \varepsilon_{adj}\right) * C * B_2 * F_2(\boldsymbol{\lambda}) \quad (9)$$

We opt here to be conservative and reduce the amount of fluorescence from direct excitation of fluorescent protein 2 by the FRET taking place.

For MuSIC probes with three fluorescent proteins, called 1, 2, and 3 ordered from blue to red, the emission intensity depends on six different components. Three are due to direct excitation: emission intensity of fluorescent protein 1 (I_1), emission intensity of fluorescent protein 2 (I_2), and emission intensity of fluorescent protein 3 (I_3). The other three are due to FRET: FRET sensitized emission intensity of fluorescent protein 2 due to FRET with fluorescent protein 1 ($I_{2,1}$), FRET sensitized emission intensity of fluorescent protein 3 due to FRET with fluorescent protein 2 that ultimately came from FRET with fluorescent protein 1 ($I_{3,1}$), and FRET sensitized emission intensity of fluorescent protein 3 due to FRET with fluorescent protein 2 ($I_{3,2}$). The overall intensity is calculated as the sum of the six intensities. We assume negligible direct FRET from fluorescent protein 1 to 3.

$$I = I_1 + I_2 + I_3 + I_{2,1} + I_{3,1} + I_{3,2}$$

(10)

The adjusted FRET efficiencies between fluorescent proteins, ε_{adj1} and ε_{adj2}, are calculated as above

$$\varepsilon_{adj_1} = \varepsilon_1 * \left(1 - E_2(\lambda_{ex})\right)$$

(11)

$$\varepsilon_{adj_2} = \varepsilon_2 * \left(1 - E_3(\lambda_{ex})\right)$$

(12)

The emission intensity of fluorescent protein 1 due to direct excitation is calculated by

$$I_1(\boldsymbol{\lambda}) = E_1(\lambda_{ex}) * (1 - \varepsilon_{adj1}) * C * B_1 * F_1(\boldsymbol{\lambda})$$

(13)

This emission is calculated similarly to that above and is corrected to only consider the fraction of excited fluorescent protein 1 molecules that are not undergoing FRET with fluorescent protein 2.

The emission intensity of fluorescent protein 2 due to direct excitation is calculated by

$$I_2(\boldsymbol{\lambda}) = E_2(\lambda_{ex}) * (1 - \varepsilon_{adj_1} - \varepsilon_{adj_2}) * C * B_2 * F_2(\boldsymbol{\lambda})$$

(14)

This emission is corrected to only consider the fraction of excited fluorescent protein 2 molecules that are not undergoing FRET with either fluorescent proteins 1 or 3.

The emission intensity of fluorescent protein 3 due to direct excitation is calculated by

$$I_3(\boldsymbol{\lambda}) = E_3(\lambda_{ex}) * \left(1 - \varepsilon_{adj_2} - \varepsilon_{adj_1} * \varepsilon_{adj_2}\right) * C * B_3 * F_3(\boldsymbol{\lambda})$$

(15)

This emission intensity only considers the fraction of fluorescent protein 3 molecules that are not involved in FRET with either fluorescent protein 2 or FRET from the first fluorescent protein through the second.

The emission intensity of fluorescent protein 2 due to FRET from fluorescent protein 1 is calculated by

$$I_{2,1}(\boldsymbol{\lambda}) = E_1(\lambda_{ex}) * \varepsilon_{adj_1} * C * B_2 * F_2(\boldsymbol{\lambda})$$

(16)

The emission intensity of fluorescent protein 3 due to FRET from fluorescent protein 1 through fluorescent protein 2 is calculated by

$$I_{3,1}(\boldsymbol{\lambda}) = E_1(\lambda_{ex}) * \varepsilon_{adj_1} * \varepsilon_{adj_2} * C * B_3 * F_3(\boldsymbol{\lambda})$$

(17)

Finally, the emission intensity of fluorescent protein 3 due to FRET from fluorescent protein 2 is calculated as follows

$$I_{3,2}(\boldsymbol{\lambda}) = E_2(\lambda_{ex}) * \varepsilon_{adj_2} * C * B_3 * F_3(\boldsymbol{\lambda})$$

(18)

Calculating the Observed Spectra Using Cytek Binning. The emission spectra of the MuSIC probes are simulated at every nm as described above. To best replicate the emission spectra generated from the Cytek Northern Lights and the Cytek Aurora flow cytometers, we condensed the simulated emission spectra based on the emission channels for each instrument, referred to as binning. Each emission channel represents spectral data condensed over a range of wavelengths, so to convert the simulated emission spectra (which is at every nm) we averaged the simulated emission spectra *I* for each probe over the wavelength ranges of each instrument's emission channels. Each binned emission point is calculated as follows

$$f_j = \frac{\sum_i I_{ji}}{n_j}$$

(19)

Where f_j is the binned emission point over the wavelength range for channel *j*, *n* is the number of wavelengths in channel *j*, and *I* is calculated as above.

Noise Model. Noise is assumed to be normally distributed and simulated using the MATLAB function `randn`. The standard deviation for the normal distribution is estimated based on data from the Cytek Northern Lights flow cytometer, given by the manufacturer, which is estimated at 50 relative fluorescent units (RFUs) for an intensity of 10^5 RFUs. In the above simulations, the fluorescence emission spectra have an average maximum of ~10 RFUs. The standard deviation of 50 is thus decreased by a factor of 10^4 to adjust for the simulated emission spectra, giving a standard deviation of 0.005 for noise. This value is used as the value for "low" noise. The standard deviation is set to 0.05 for "high" noise (10-fold higher than the low noise).

Unmixing. The fluorescence emission spectra of a mixture of fluorophores can be cast as a sum of the emission spectra of the individual fluorophores as follows.

$$\boldsymbol{\mu} = \boldsymbol{R} \cdot \boldsymbol{c} \qquad (20)$$

Where $\boldsymbol{\mu}$ is an *n-by-1* vector of observed fluorescence emission intensity at *n* emission wavelength/excitation channel combinations, **R** is an *n-by-m* reference matrix that is generated from the simulated emission spectra of *m* individual probes with multiple excitation channels as described above, and $\boldsymbol{c}$ is an *m-by-1* vector containing the relative probe concentrations.

Solving this equation gives an estimate of the relative probe concentrations, $\boldsymbol{c}$. This is done using the MATLAB function `lsqlin`. The lower bound for elements of $\boldsymbol{c}$ is set to zero, and the upper bound is left empty.

Generating a Simulated Experimental Data Set. Simulated data are generated by first specifying the relative probe concentrations for different mixtures of MuSIC probes. This is referred to as the actual mixture composition vector, $\mathbf{c_a}$. For single probe mixtures, one probe concentration is set to 1 and all others are zero. For barcode mixtures, two probe concentrations are set to 1, and all others are zero. For two barcode mixtures, four probe concentrations are set to 1, and all others are zero. For the case of variable probe expression levels, probe concentrations are set to a random number between 0.5-1.5 (`rand`). For two barcode mixtures, the probes are divided into two batches, and two probes are chosen from the first batch while two are chosen from the second (see Results). Equation 20 with $\mathbf{c_a}$ and **R** is used to calculate $\boldsymbol{\mu_a}$, the simulated emission spectra of the mixture. Experimental noise is then added to the simulated emission spectra at either low or high levels, as described above, giving $\boldsymbol{\mu_n}$, the simulated observed spectra. Finally, Equation 20 is used to solve for **c** (i.e., unmixing), giving the predicted mixture composition, $\hat{\mathbf{c}}$.

Binary Classification. Binary classification is performed on the predicted mixture composition vector by converting the relative level for each probe to a one or zero based on a threshold for each probe. The threshold for each probe is determined as that which gives the

maximum Matthews Correlation Coefficient value for each probe respectively based on simulation data (see below).

Confusion Matrix and Matthews Correlation Coefficient (MCC). Evaluating binary classification performance requires the calculation of a confusion matrix, which serves as a centralized table that tracks the number of true and false positive and negative classifications. The confusion matrix allows for the calculation of a multitude of performance metrics and is calculated using the MATLAB function `confusionmat.m`. Out of these different metrics, the Matthew's Correlation Coefficient (MCC), or phi coefficient, was chosen to quantify the performance of probes in the simulations. The MCC was chosen because it is appropriate when the classes are highly imbalanced[42], such as what we have here when there are many more true negatives than true positives. Other metrics, such as the F1 score or Accuracy, are problematic for situations where there might be significantly more true negatives than false positives.

Given a classification threshold to evaluate, a confusion matrix is generated for each probe using the actual mixture compositions and the binary predicted probe concentrations for each probe. These confusion matrices are used to generate an individual MCC score for each probe, given the threshold. The threshold is then varied to determine the optimum threshold to maximize MCC for a particular probe.

A confusion matrix is generated for the entire group of probes using a matrix of all concatenated actual mixture composition vectors and a matrix of all concatenated predicted mixture composition vectors. This confusion matrix is used to generate the overall MCC score which represents the performance for the entire group of probes.

Results

This paper explores a theory for creating a large library of genetically-encoded, fluorescence spectral barcodes for potential application to genetic interaction screening. It is based on our recently published Multiplexing using Spectral Imaging and Combinatorics (MuSIC) approach[33], which creates unique spectral signatures from stably-linked combinations of individual fluorophores. The individual fluorophores or combinations are called MuSIC probes. In this work, we consider expanding the number of fluorophores used by fusing 2 or 3 individual fluorophores that would give rise to unique spectral properties. The spectral signatures of combination probes are linearly independent (i.e., unique) from the individual fluorophore spectra comprising the combination so long as sufficient Förster resonance energy transfer (FRET) occurs. This linear independence property allows for the estimation of individual MuSIC probe levels when they are together in a mixture, a process often called "unmixing".

We selected 18 fluorescent proteins (see Methods and **Table S1**) that span the ultraviolet to infrared spectrum and first wanted to determine how many MuSIC probes could be generated. The quality of unmixing depends on the FRET efficiency, which is directly related to the Förster radius and the physical distance between chromophores of the fluorescent proteins (see Methods). The distance between fluorescent proteins can usually be adjusted by altering the length and nature of the peptide fusion linker; thus, the answer to this question depends on the Förster radius chosen as acceptable (**Fig. 1A-B**). Since high FRET producing pairs usually have a Förster radius greater than 5 nm[40], we only consider MuSIC probes that have an estimated Förster radius greater than 5 nm. At this cutoff, 910 MuSIC probes can be generated (**Table S2**), but this is far from genome-scale. We should also note here that in principle the same fluorescent proteins in a probe could be engineered to be a different distance apart and thus a different FRET efficiency, which would increase the number of probes. However, for the purposes of this work, we only consider one FRET efficiency (~50%) per probe.

Can we develop another layer of combinatorics to generate further diversity? Consider the concept of a MuSIC barcode that is a combination of MuSIC probes. As an example, let us start with two fluorescent proteins, mAmetrine and mOrange2. From these two fluorescent proteins we can create three MuSIC probes: a single fluorescent protein probe of mAmetrine, the combination probe of mAmetrine and mOrange2, and another single fluorescent protein probe of mOrange2. A MuSIC barcode is then every 2-way combination of the probes. Thus, from these

probes we can create three MuSIC barcodes **(Fig. 1C-D)**. The MuSIC barcode spectra are clearly unique from one another. The number of barcodes that can be generated given a particular number of probes is given by combinatorics (see Methods); 910 probes gives 413,595 barcodes (**Fig. 1B, E**).

This barcode diversity far exceeds the number of genes in the human genome (**Fig. 1E**). If each MuSIC barcode could be paired to a guide RNA (gRNA), and if resolvable in practice, one could perform genome-scale genetic screening that is non-destructive in single cells. Specifically, then if a certain MuSIC barcode is detected in a particular cell (via a fluorescence emission spectra measurement), that would indicate the gRNA that was present, and therefore the target gene that was likely modulated in that cell.

MuSIC barcodes may also enable large-scale genetic interaction screening (**Fig. 1E**). Consider that a gRNA is paired to a MuSIC barcode as above, but instead there are two MuSIC barcodes in a cell corresponding to two specific gRNAs. This means four MuSIC probes would be present in the cell. To avoid mapping ambiguity from probes to barcodes to gRNA, the MuSIC probe library would have to be split in half before linking gRNA with MuSIC barcodes, which makes the predicted scale of genetic interaction screening lower than that of genetic screens. With 910 MuSIC probes, 103,285 gRNA could be studied for genetic interactions, which approaches human genome-scale genetic interaction screening at ~3x redundancy.

While the above suggests MuSIC barcodes may enable novel genetic screening technology, how well might it work in practice? Of the 910 potential probes, how many can reliably be identified from expected mixtures? To constrain the answer to this question, we developed a simulation workflow. Rapid measurement of fluorescence emission spectra in single cells has recently become possible with Cytek flow cytometers. For this reason, we have based the simulation studies described in this paper off the Cytek Northern Lights Flow Cytometer (3 lasers; 405, 488, and 635nm) and the Cytek Aurora Flow Cytometer (5 lasers; 356, 405, 488, 561, and 635nm) **(Fig. 2A)**. The spectral emission bin structure for each instrument and its signal-to-noise ratio is known and we incorporate such information into our simulated measurements (**Fig. 2A—**see also Methods). For genetic screens, it can be useful to reserve one excitation channel to measure an observed phenotype. Therefore, we also investigated a setup for 2 lasers (Northern Lights, dedicating the 635nm laser to a phenotype) and 4 lasers (Aurora, dedicating 635nm laser to phenotype) **(Fig. 2B**).

We implemented the following simulation strategy to eliminate "poorly" performing probes from consideration **(Fig. 3A).** A "poorly" performing probe is one that leads to at least one misclassification event in simulations. At the core of the algorithm is a simulated MuSIC probe mixture. This is a vector that represents which probe or probe(s) are present in the ground truth, which we call the actual mixture composition. Using the actual mixture composition vector and the calculated reference matrix (see Methods—spectra of individual probes), we can calculate the emission spectra of the mixture. We add low or high noise (see Methods—based on Cytek flow cytometer specs) to the emission spectra of the mixture, generating the simulated observed spectra. After noise is added, we perform linear unmixing, which generates the predicted mixture composition. To compare the predicted mixture composition to the actual mixture composition, we first perform binary classification (see Methods). To quantify performance, we calculate the Matthews correlation coefficient, which is suitable for cases such as this where there are many more true negatives than true positives. If overall classification is not perfect (MCC < 1), then we identify which probe has the worst MCC, and remove it. The simulation is repeated until overall classification is perfect **(Fig. 3B)**, at which point we obtain the final list of good probes (**Table S2**). This process is performed in triplicate.

We use three sequential sets of simulations to determine a list of "good" MuSIC probes that can be used (1) on their own, (2) for MuSIC barcodes (genetic screening), and (3) for two MuSIC barcodes (genetic interaction screening) (**Table S2**). The final list that is obtained in Simulation 1 is used for Simulation 2, and likewise 2 for 3 (**Fig. 3C**). For example, only probes that are good for use on their own are considered for MuSIC barcodes. The list of "good" MuSIC probes from Simulation 2 sets constraints on genetic screening for single gene effects and the list of good MuSIC probes from Simulation 3 sets constraints on genetic interaction screening.

The results of this process are summarized in **Table 1.** The final number of good MuSIC probes that can be unmixed with perfect classification for MuSIC barcodes and sets of two MuSIC barcodes are listed for each of the experimental setups (summarized in **Fig. 2B**). We found reasonable overlap between which probes were labeled as good between replicate runs (**Fig. S1**), although the overall number of probes seems to be a more reproducible and larger factor (**Table 1**). Given these results, the number of gRNA that can be used for genetic and genetic interaction screening are calculated from **Fig 1E**. In general, more lasers and lower noise allows for more probes and barcodes, as expected. For genetic screens, each scenario

investigated suggested potential for genome-scale operation. For genetic interaction screens, 4 and 5 laser setups with low noise predicted operation at genome-scale. Even 2 and 3 laser setups with high noise predicted operation with 1000s of gRNA in genetic interaction screens, an order of magnitude above current methods. If we consider typical ranges of cell-to-cell variability in probe expression levels, then we can still generate gRNA on the same scale (**Table S3**). If we only consider MuSIC probes with one or two fluorescent proteins, as opposed to three, we can still achieve multiple hundred gRNA for genetic interaction screens (**Table S4**). Overall, these results suggest MuSIC barcoding theory represents a promising approach to transforming genetic perturbation technology.

Discussion

Here we propose an approach for single-cell, non-destructive, and potentially genome-scale genetic and genetic interaction screens. This work builds on our recently developed theory for Multiplexing using Spectral Imaging and Combinatorics (MuSIC). MuSIC probes are stably linked combinations of fluorophores with unique spectral signatures that can be deconvolved when in a mixture with other MuSIC probes. The novel concept introduced in this work is that of a MuSIC barcode, a combination of MuSIC probes. Given currently available fluorescent proteins, we estimate that ~10^5 unique MuSIC barcodes can be created from combinations of MuSIC probes. We devised a simulation workflow to generate lists of MuSIC probes that are likely to be deconvolvable in a mixture, given binary classification applications. These results show the potential for genetic screens at the human genome-scale and genetic interaction screens for at least 1000s of genes. In some cases (i.e. 4 or 5 lasers and low noise), results show the potential to perform genetic interaction screens at a human genome-scale.

What could be learned with non-destructive, single-cell genetic screens? When analyses are done on a single-cell level, each cell is analyzed independently, and as a result, multiple measurements can be done in parallel, increasing throughput[43–45]. To accomplish this, CRISPR screenings have been paired with single-cell RNA sequencing using methods like Perturb-Seq[46], CRISP-seq[47], or CROP-seq[48,49]. While single-cell sequencing has the ability to pair transcriptome responses to a nucleic acid barcode that indicates the genetic perturbation, it is as yet prohibitively expensive for covering interaction space[50,51]. Moreover, sequencing is a destructive technology so one cannot subsequently study perturbed cells-of-interest. The use of MuSIC barcodes could expand on the capabilities of these methods by allowing for high throughput genetic screening in a non-destructive manner. A non-destructive application in single live cells could allow sorting of rare cell types for subsequent follow-up studies. This could lead to co-isolating rare cell types thought to cooperate with each other for a disease phenotype.

What could be explored with high-dimensional non-destructive genetic interaction screens? One application is synthetic lethal interactions, which is defined as a genetic interaction that results in cell death, but disruption of the individual genes does not. Synthetic lethality has previously led to the discovery that poly(ADP-ribose) polymerase (PARP) inhibitors effectively kill BRCA1- and BRCA2 mutant tumor cells in breast cancer[52]. The proposed method may allow

for genetic interaction screening at a near genome-scale, which could lead to the discovery of new synthetic lethal interactions in a high-throughput manner that is not currently possible. By discovering and exploiting synthetic lethal interactions in cancer cells, combinations of drugs can be used to treat cancer more effectively and at lower drug concentrations and thus lower toxicity[54].

Although simulations suggest a large potential for the approach when applied to genetic screening, there are multiple technical hurdles to its implementation. How can one clone thousands of unique MuSIC barcodes specifically paired with matched gRNA? If one uses lentiviruses to deliver the constructs, how does one avoid template switching between genetically similar fluorescent proteins or barcodes, corrupting the connection between the barcode and gRNA[55]? The constructs may be large as well, so how does one achieve high enough titer to perform genetic interaction screening? Although flow cytometry is fast, can one assay enough cells to adequately explore gene interaction space? These are just some of the major issues that will arise, yet the potential applications, if these issues can be overcome, could be highly impactful.

Although we focused here on genetic screening as an application, genome-scale spectral barcode libraries could have other uses, such as high-dimensional cell lineage tracing. Current fluorescence-based lineage tracking is limited from spectral overlap and the number of unique probes. Techniques such as Brainbow work to fill this gap by using random ratios of different fluorophores to label cells[56], but are still limited to ~10s of deconvolvable colors[57]. This has been partially overcome through the use of DNA barcodes in each cell but requires destructive DNA sequencing to be deconvovled[57]. Music barcodes could be used to bridge this gap by expanding the available palette of color codes for fluorescence-based lineage tracing to potentially thousands of deconvolvable colors.

In conclusion, despite impending technical hurdles, the simulation studies presented here show the potential for MuSIC barcodes to enable high-dimensional genetic interaction screens at the human genome-scale. Its single-cell resolution compatibility and non-destructive features could also enable multiple new applications for established genetic screening, or for cell lineage tracking. The capabilities of this approach can further be increased by increasing the number of excitation lasers and/or the spectral wavelength resolution.

References

(1) Wang Tim; Wei Jenny J.; Sabatini David M.; Lander Eric S. Genetic Screens in Human Cells Using the CRISPR-Cas9 System. *Science* **2014**, *343* (6166), 80–84. https://doi.org/10.1126/science.1246981.

(2) Xue, H.-Y.; Ji, L.-J.; Gao, A.-M.; Liu, P.; He, J.-D.; Lu, X.-J. CRISPR-Cas9 for Medical Genetic Screens: Applications and Future Perspectives. *J. Med. Genet.* **2016**, *53* (2), 91. https://doi.org/10.1136/jmedgenet-2015-103409.

(3) Wei, L.; Lee, D.; Law, C.-T.; Zhang, M. S.; Shen, J.; Chin, D. W.-C.; Zhang, A.; Tsang, F. H.-C.; Wong, C. L.-S.; Ng, I. O.-L.; Wong, C. C.-L.; Wong, C.-M. Genome-Wide CRISPR/Cas9 Library Screening Identified PHGDH as a Critical Driver for Sorafenib Resistance in HCC. *Nat. Commun.* **2019**, *10* (1), 4681. https://doi.org/10.1038/s41467-019-12606-7.

(4) Giaever, G.; Chu, A. M.; Ni, L.; Connelly, C.; Riles, L.; Véronneau, S.; Dow, S.; Lucau-Danila, A.; Anderson, K.; André, B.; Arkin, A. P.; Astromoff, A.; El Bakkoury, M.; Bangham, R.; Benito, R.; Brachat, S.; Campanaro, S.; Curtiss, M.; Davis, K.; Deutschbauer, A.; Entian, K.-D.; Flaherty, P.; Foury, F.; Garfinkel, D. J.; Gerstein, M.; Gotte, D.; Güldener, U.; Hegemann, J. H.; Hempel, S.; Herman, Z.; Jaramillo, D. F.; Kelly, D. E.; Kelly, S. L.; Kötter, P.; LaBonte, D.; Lamb, D. C.; Lan, N.; Liang, H.; Liao, H.; Liu, L.; Luo, C.; Lussier, M.; Mao, R.; Menard, P.; Ooi, S. L.; Revuelta, J. L.; Roberts, C. J.; Rose, M.; Ross-Macdonald, P.; Scherens, B.; Schimmack, G.; Shafer, B.; Shoemaker, D. D.; Sookhai-Mahadeo, S.; Storms, R. K.; Strathern, J. N.; Valle, G.; Voet, M.; Volckaert, G.; Wang, C.; Ward, T. R.; Wilhelmy, J.; Winzeler, E. A.; Yang, Y.; Yen, G.; Youngman, E.; Yu, K.; Bussey, H.; Boeke, J. D.; Snyder, M.; Philippsen, P.; Davis, R. W.; Johnston, M. Functional Profiling of the Saccharomyces Cerevisiae Genome. *Nature* **2002**, *418* (6896), 387–391. https://doi.org/10.1038/nature00935.

(5) Trigos, A. S.; Pearson, R. B.; Papenfuss, A. T.; Goode, D. L. Altered Interactions between Unicellular and Multicellular Genes Drive Hallmarks of Transformation in a Diverse Range of Solid Tumors. *Proc. Natl. Acad. Sci. U. S. A.* **2017**, *114* (24), 6406–6411. https://doi.org/10.1073/pnas.1617743114.

(6) Forsburg, S. L. The Art and Design of Genetic Screens: Yeast. *Nat. Rev. Genet.* **2001**, *2* (9), 659–668. https://doi.org/10.1038/35088500.

(7) Mager, W. H.; Winderickx, J. Yeast as a Model for Medical and Medicinal Research. *Trends Pharmacol. Sci.* **2005**, *26* (5), 265–273. https://doi.org/10.1016/j.tips.2005.03.004.

(8) Chen, L.; Wang, Z.; Ghosh-Roy, A.; Hubert, T.; Yan, D.; O'Rourke, S.; Bowerman, B.; Wu, Z.; Jin, Y.; Chisholm, A. D. Axon Regeneration Pathways Identified by Systematic Genetic Screening in C. Elegans. *Neuron* **2011**, *71* (6), 1043–1057. https://doi.org/10.1016/j.neuron.2011.07.009.

(9) Urnov, F. D.; Rebar, E. J.; Holmes, M. C.; Zhang, H. S.; Gregory, P. D. Genome Editing with Engineered Zinc Finger Nucleases. *Nat. Rev. Genet.* **2010**, *11* (9), 636–646. https://doi.org/10.1038/nrg2842.

(10) Joung, J. K.; Sander, J. D. TALENs: A Widely Applicable Technology for Targeted Genome Editing. *Nat. Rev. Mol. Cell Biol.* **2013**, *14* (1), 49–55. https://doi.org/10.1038/nrm3486.

(11) Novina, C. D.; Sharp, P. A. The RNAi Revolution. *Nature* **2004**, *430* (6996), 161–164. https://doi.org/10.1038/430161a.

(12) Shalem Ophir; Sanjana Neville E.; Hartenian Ella; Shi Xi; Scott David A.; Mikkelsen Tarjei S.; Heckl Dirk; Ebert Benjamin L.; Root David E.; Doench John G.; Zhang Feng. Genome-Scale CRISPR-Cas9 Knockout Screening in Human Cells. *Science* **2014**, *343* (6166), 84–87. https://doi.org/10.1126/science.1247005.

(13) Mali Prashant; Yang Luhan; Esvelt Kevin M.; Aach John; Guell Marc; DiCarlo James E.; Norville Julie E.; Church George M. RNA-Guided Human Genome Engineering via Cas9. *Science* **2013**, *339* (6121), 823–826. https://doi.org/10.1126/science.1232033.

(14) Schmid-Burgk, J. L. Disruptive Non-Disruptive Applications of CRISPR/Cas9. *Chem. Biotechnol. • Pharm. Biotechnol.* **2017**, *48*, 203–209. https://doi.org/10.1016/j.copbio.2017.06.001.

(15) Kampmann, M. CRISPRi and CRISPRa Screens in Mammalian Cells for Precision Biology and Medicine. *ACS Chem. Biol.* **2018**, *13* (2), 406–416. https://doi.org/10.1021/acschembio.7b00657.

(16) Baryshnikova, A.; Costanzo, M.; Kim, Y.; Ding, H.; Koh, J.; Toufighi, K.; Youn, J.-Y.; Ou, J.; San Luis, B.-J.; Bandyopadhyay, S.; Hibbs, M.; Hess, D.; Gingras, A.-C.; Bader, G. D.; Troyanskaya, O. G.; Brown, G. W.; Andrews, B.; Boone, C.; Myers, C. L. Quantitative Analysis of Fitness and Genetic Interactions in Yeast on a Genome Scale. *Nat. Methods* **2010**, *7* (12), 1017–1024. https://doi.org/10.1038/nmeth.1534.

(17) Behan, F. M.; Iorio, F.; Picco, G.; Gonçalves, E.; Beaver, C. M.; Migliardi, G.; Santos, R.; Rao, Y.; Sassi, F.; Pinnelli, M.; Ansari, R.; Harper, S.; Jackson, D. A.; McRae, R.; Pooley, R.; Wilkinson, P.; van der Meer, D.; Dow, D.; Buser-Doepner, C.; Bertotti, A.; Trusolino, L.; Stronach, E. A.; Saez-Rodriguez, J.; Yusa, K.; Garnett, M. J. Prioritization of Cancer Therapeutic Targets Using CRISPR–Cas9 Screens. *Nature* **2019**, *568* (7753), 511–516. https://doi.org/10.1038/s41586-019-1103-9.

(18) Costanzo, M.; Baryshnikova, A.; Myers, C. L.; Andrews, B.; Boone, C. Charting the Genetic Interaction Map of a Cell. *Anal. Biotechnol.* **2011**, *22* (1), 66–74. https://doi.org/10.1016/j.copbio.2010.11.001.

(19) Shen, J. P.; Zhao, D.; Sasik, R.; Luebeck, J.; Birmingham, A.; Bojorquez-Gomez, A.; Licon, K.; Klepper, K.; Pekin, D.; Beckett, A. N.; Sanchez, K. S.; Thomas, A.; Kuo, C.-C.; Du, D.; Roguev, A.; Lewis, N. E.; Chang, A. N.; Kreisberg, J. F.; Krogan, N.; Qi, L.; Ideker, T.; Mali, P. Combinatorial CRISPR–Cas9 Screens for de Novo Mapping of Genetic Interactions. *Nat. Methods* **2017**, *14* (6), 573–576. https://doi.org/10.1038/nmeth.4225.

(20) Kuzmin Elena; VanderSluis Benjamin; Wang Wen; Tan Guihong; Deshpande Raamesh; Chen Yiqun; Usaj Matej; Balint Attila; Mattiazzi Usaj Mojca; van Leeuwen Jolanda; Koch Elizabeth N.; Pons Carles; Dagilis Andrius J.; Pryszlak Michael; Wang Jason Zi Yang; Hanchard Julia; Riggi Margot; Xu Kaicong; Heydari Hamed; San Luis Bryan-Joseph; Shuteriqi Ermira; Zhu Hongwei; Van Dyk Nydia; Sharifpoor Sara; Costanzo Michael; Loewith Robbie; Caudy Amy; Bolnick Daniel; Brown Grant W.; Andrews Brenda J.; Boone Charles; Myers Chad L. Systematic Analysis of Complex Genetic Interactions. *Science* **2018**, *360* (6386), eaao1729. https://doi.org/10.1126/science.aao1729.

(21) Mani, R.; St.Onge, R. P.; Hartman, J. L.; Giaever, G.; Roth, F. P. Defining Genetic Interaction. *Proc. Natl. Acad. Sci.* **2008**, *105* (9), 3461. https://doi.org/10.1073/pnas.0712255105.

(22) Dixon, S. J.; Costanzo, M.; Baryshnikova, A.; Andrews, B.; Boone, C. Systematic Mapping of Genetic Interaction Networks. *Annu. Rev. Genet.* **2009**, *43* (1), 601–625. https://doi.org/10.1146/annurev.genet.39.073003.114751.

(23) Puddu, F.; Herzog, M.; Selivanova, A.; Wang, S.; Zhu, J.; Klein-Lavi, S.; Gordon, M.; Meirman, R.; Millan-Zambrano, G.; Ayestaran, I.; Salguero, I.; Sharan, R.; Li, R.; Kupiec, M.; Jackson, S. P. Genome Architecture and Stability in the Saccharomyces Cerevisiae Knockout Collection. *Nature* **2019**, *573* (7774), 416–420. https://doi.org/10.1038/s41586-019-1549-9.

(24) Hedges, S. B. The Origin and Evolution of Model Organisms. *Nat. Rev. Genet.* **2002**, *3* (11), 838–849. https://doi.org/10.1038/nrg929.

(25) Du, D.; Roguev, A.; Gordon, D. E.; Chen, M.; Chen, S.-H.; Shales, M.; Shen, J. P.; Ideker, T.; Mali, P.; Qi, L. S.; Krogan, N. J. Genetic Interaction Mapping in Mammalian Cells Using CRISPR Interference. *Nat. Methods* **2017**, *14* (6), 577–580. https://doi.org/10.1038/nmeth.4286.

(26) Wong, A. S. L.; Choi, G. C. G.; Cui, C. H.; Pregernig, G.; Milani, P.; Adam, M.; Perli, S. D.; Kazer, S. W.; Gaillard, A.; Hermann, M.; Shalek, A. K.; Fraenkel, E.; Lu, T. K. Multiplexed Barcoded CRISPR-Cas9 Screening Enabled by CombiGEM. *Proc. Natl. Acad. Sci.* **2016**, *113* (9), 2544. https://doi.org/10.1073/pnas.1517883113.

(27) Han, K.; Jeng, E. E.; Hess, G. T.; Morgens, D. W.; Li, A.; Bassik, M. C. Synergistic Drug Combinations for Cancer Identified in a CRISPR Screen for Pairwise Genetic Interactions. *Nat. Biotechnol.* **2017**, *35* (5), 463–474. https://doi.org/10.1038/nbt.3834.

(28) Kim, G. B.; Dutra-Clarke, M.; Levy, R.; Park, H.; Sabet, S.; Molina, J.; Akhtar, A. A.; Danielpour, M.; Breunig, J. TMOD-08. INVESTIGATING PEDIATRIC GBM USING IN VIVO SOMATIC MOUSE MOSAICS WITH LOCUS-SPECIFIC, STABLY-INTEGRATED TRANSGENIC ELEMENTS. *Neuro-Oncol.* **2017**, *19* (Suppl 4), iv50–iv50. https://doi.org/10.1093/neuonc/nox083.207.

(29) Wroblewska, A.; Dhainaut, M.; Ben-Zvi, B.; Rose, S. A.; Park, E. S.; Amir, E.-A. D.; Bektesevic, A.; Baccarini, A.; Merad, M.; Rahman, A. H.; Brown, B. D. Protein Barcodes Enable High-Dimensional Single-Cell CRISPR Screens. *Cell* **2018**, *175* (4), 1141-1155.e16. https://doi.org/10.1016/j.cell.2018.09.022.

(30) Schraivogel, D.; Gschwind, A. R.; Milbank, J. H.; Leonce, D. R.; Jakob, P.; Mathur, L.; Korbel, J. O.; Merten, C. A.; Velten, L.; Steinmetz, L. M. Targeted Perturb-Seq Enables Genome-Scale Genetic Screens in Single Cells. *Nat. Methods* **2020**, *17* (6), 629–635. https://doi.org/10.1038/s41592-020-0837-5.

(31) Dixit, A.; Parnas, O.; Li, B.; Chen, J.; Fulco, C. P.; Jerby-Arnon, L.; Marjanovic, N. D.; Dionne, D.; Burks, T.; Raychowdhury, R.; Adamson, B.; Norman, T. M.; Lander, E. S.; Weissman, J. S.; Friedman, N.; Regev, A. Perturb-Seq: Dissecting Molecular Circuits with Scalable Single-Cell RNA Profiling of Pooled Genetic Screens. *Cell* **2016**, *167* (7), 1853-1866.e17. https://doi.org/10.1016/j.cell.2016.11.038.

(32) Ursu, O.; Neal, J. T.; Shea, E.; Thakore, P. I.; Jerby-Arnon, L.; Nguyen, L.; Dionne, D.; Diaz, C.; Bauman, J.; Mosaad, M. M.; Fagre, C.; Lo, A.; McSharry, M.; Giacomelli, A. O.; Ly, S. H.; Rozenblatt-Rosen, O.; Hahn, W. C.; Aguirre, A. J.; Berger, A. H.; Regev, A.; Boehm, J. S. Massively Parallel Phenotyping of Coding Variants in Cancer with Perturb-Seq. *Nat. Biotechnol.* **2022**, *40* (6), 896–905. https://doi.org/10.1038/s41587-021-01160-7.

(33) Holzapfel, H. Y.; Stern, A. D.; Bouhaddou, M.; Anglin, C. M.; Putur, D.; Comer, S.; Birtwistle, M. R. Fluorescence Multiplexing with Spectral Imaging and Combinatorics. *ACS Comb. Sci.* **2018**, *20* (11), 653–659. https://doi.org/10.1021/acscombsci.8b00101.

(34) Kremers, G.-J.; Goedhart, J.; van Munster, E. B.; Gadella, T. W. J. Cyan and Yellow Super Fluorescent Proteins with Improved Brightness, Protein Folding, and FRET Förster Radius,. *Biochemistry* **2006**, *45* (21), 6570–6580. https://doi.org/10.1021/bi0516273.

(35) Piston, D. W.; Kremers, G.-J. Fluorescent Protein FRET: The Good, the Bad and the Ugly. *Trends Biochem. Sci.* **2007**, *32* (9), 407–414. https://doi.org/10.1016/j.tibs.2007.08.003.

(36) Vogel, S. S.; van der Meer, B. W.; Blank, P. S. Estimating the Distance Separating Fluorescent Protein FRET Pairs. *Adv. Light Microsc.* **2014**, *66* (2), 131–138. https://doi.org/10.1016/j.ymeth.2013.06.021.

(37) Basak, S.; Saikia, N.; Dougherty, L.; Guo, Z.; Wu, F.; Mindlin, F.; Lary, J. W.; Cole, J. L.; Ding, F.; Bowen, M. E. Probing Interdomain Linkers and Protein Supertertiary Structure In Vitro and in Live Cells with Fluorescent Protein Resonance Energy Transfer. *J. Mol. Biol.* **2021**, *433* (5), 166793. https://doi.org/10.1016/j.jmb.2020.166793.

(38) Day, R. N.; Booker, C. F.; Periasamy, A. Characterization of an Improved Donor Fluorescent Protein for Forster Resonance Energy Transfer Microscopy. *J. Biomed. Opt.* **2008**, *13* (3), 031203–031203. https://doi.org/10.1117/1.2939094.

(39) George Abraham, B.; Sarkisyan, K. S.; Mishin, A. S.; Santala, V.; Tkachenko, N. V.; Karp, M. Fluorescent Protein Based FRET Pairs with Improved Dynamic Range for Fluorescence Lifetime Measurements. *PloS One* **2015**, *10* (8), e0134436–e0134436. https://doi.org/10.1371/journal.pone.0134436.

(40) Bajar, B. T.; Wang, E. S.; Zhang, S.; Lin, M. Z.; Chu, J. A Guide to Fluorescent Protein FRET Pairs. *Sensors* **2016**, *16* (9), 1488. https://doi.org/10.3390/s16091488.

(41) Schwartz, A.; Wang, L.; Early, E.; Gaigalas, A.; Zhang, Y.-Z.; Marti, G. E.; Vogt, R. F. Quantitating Fluorescence Intensity from Fluorophore: The Definition of MESF Assignment. *J. Res. Natl. Inst. Stand. Technol.* **2002**, *107* (1), 83–91. https://doi.org/10.6028/jres.107.009.

(42) Boughorbel, S.; Jarray, F.; El-Anbari, M. Optimal Classifier for Imbalanced Data Using Matthews Correlation Coefficient Metric. *PloS One* **2017**, *12* (6), e0177678–e0177678. https://doi.org/10.1371/journal.pone.0177678.

(43) Norman Thomas M.; Horlbeck Max A.; Replogle Joseph M.; Ge Alex Y.; Xu Albert; Jost Marco; Gilbert Luke A.; Weissman Jonathan S. Exploring Genetic Interaction Manifolds Constructed from Rich Single-Cell Phenotypes. *Science* **2019**, *365* (6455), 786–793. https://doi.org/10.1126/science.aax4438.

(44) Gilbert Luke A. Mapping Cancer Genetics at Single-Cell Resolution. *Sci. Transl. Med.* **2020**, *12* (558), eabd3049. https://doi.org/10.1126/scitranslmed.abd3049.

(45) Liberali, P.; Snijder, B.; Pelkmans, L. Single-Cell and Multivariate Approaches in Genetic Perturbation Screens. *Nat. Rev. Genet.* **2015**, *16* (1), 18–32. https://doi.org/10.1038/nrg3768.

(46) Adamson, B.; Norman, T. M.; Jost, M.; Cho, M. Y.; Nuñez, J. K.; Chen, Y.; Villalta, J. E.; Gilbert, L. A.; Horlbeck, M. A.; Hein, M. Y.; Pak, R. A.; Gray, A. N.; Gross, C. A.; Dixit, A.; Parnas, O.; Regev, A.; Weissman, J. S. A Multiplexed Single-Cell CRISPR Screening

Platform Enables Systematic Dissection of the Unfolded Protein Response. *Cell* **2016**, *167* (7), 1867-1882.e21. https://doi.org/10.1016/j.cell.2016.11.048.

(47) Jaitin, D. A.; Weiner, A.; Yofe, I.; Lara-Astiaso, D.; Keren-Shaul, H.; David, E.; Salame, T. M.; Tanay, A.; van Oudenaarden, A.; Amit, I. Dissecting Immune Circuits by Linking CRISPR-Pooled Screens with Single-Cell RNA-Seq. *Cell* **2016**, *167* (7), 1883-1896.e15. https://doi.org/10.1016/j.cell.2016.11.039.

(48) Datlinger, P.; Rendeiro, A. F.; Schmidl, C.; Krausgruber, T.; Traxler, P.; Klughammer, J.; Schuster, L. C.; Kuchler, A.; Alpar, D.; Bock, C. Pooled CRISPR Screening with Single-Cell Transcriptome Readout. *Nat. Methods* **2017**, *14* (3), 297–301. https://doi.org/10.1038/nmeth.4177.

(49) Duan, B.; Zhou, C.; Zhu, C.; Yu, Y.; Li, G.; Zhang, S.; Zhang, C.; Ye, X.; Ma, H.; Qu, S.; Zhang, Z.; Wang, P.; Sun, S.; Liu, Q. Model-Based Understanding of Single-Cell CRISPR Screening. *Nat. Commun.* **2019**, *10* (1), 2233. https://doi.org/10.1038/s41467-019-10216-x.

(50) Ziegenhain, C.; Vieth, B.; Parekh, S.; Reinius, B.; Guillaumet-Adkins, A.; Smets, M.; Leonhardt, H.; Heyn, H.; Hellmann, I.; Enard, W. Comparative Analysis of Single-Cell RNA Sequencing Methods. *Mol. Cell* **2017**, *65* (4), 631-643.e4. https://doi.org/10.1016/j.molcel.2017.01.023.

(51) McGinnis, C. S.; Patterson, D. M.; Winkler, J.; Conrad, D. N.; Hein, M. Y.; Srivastava, V.; Hu, J. L.; Murrow, L. M.; Weissman, J. S.; Werb, Z.; Chow, E. D.; Gartner, Z. J. MULTI-Seq: Sample Multiplexing for Single-Cell RNA Sequencing Using Lipid-Tagged Indices. *Nat. Methods* **2019**, *16* (7), 619–626. https://doi.org/10.1038/s41592-019-0433-8.

(52) Ashworth, A.; Lord, C. J. Synthetic Lethal Therapies for Cancer: What's next after PARP Inhibitors? *Nat. Rev. Clin. Oncol.* **2018**, *15* (9), 564–576. https://doi.org/10.1038/s41571-018-0055-6.

(53) Parrish, P. C. R.; Thomas, J. D.; Gabel, A. M.; Kamlapurkar, S.; Bradley, R. K.; Berger, A. H. Discovery of Synthetic Lethal and Tumor Suppressor Paralog Pairs in the Human Genome. *Cell Rep.* **2021**, *36* (9), 109597. https://doi.org/10.1016/j.celrep.2021.109597.

(54) Castells-Roca, L.; Tejero, E.; Rodríguez-Santiago, B.; Surrallés, J. CRISPR Screens in Synthetic Lethality and Combinatorial Therapies for Cancer. *Cancers* **2021**, *13* (7). https://doi.org/10.3390/cancers13071591.

(55) Komatsubara, A. T.; Matsuda, M.; Aoki, K. Quantitative Analysis of Recombination between YFP and CFP Genes of FRET Biosensors Introduced by Lentiviral or Retroviral Gene Transfer. *Sci. Rep.* **2015**, *5* (1), 13283. https://doi.org/10.1038/srep13283.

(56) Weissman, T. A.; Pan, Y. A. Brainbow: New Resources and Emerging Biological Applications for Multicolor Genetic Labeling and Analysis. *Genetics* **2015**, *199* (2), 293–306. https://doi.org/10.1534/genetics.114.172510.

(57) Szu-Hsien (Sam) Wu; Ji-Hyun Lee; and Bon-Kyoung Koo. Lineage Tracing: Computational Reconstruction Goes Beyond the Limit of Imaging. *Mol. Cells* **2019**, *42* (2), 104–112. https://doi.org/10.14348/molcells.2019.0006.

Acknowledgments

The authors acknowledge funding from Clemson University, NIH/ NCI Grant R21CA196418, and NIH/NIGMS Grant R35 GM141891 . M.E.M. received funding from the Department of Education Grant P200A180076. This work was performed using the Clemson University Palmetto Super Computing Cluster.

Figure and Table Legends

Figure 1: Theory and scope of MuSIC Barcodes for genetic and genetic interaction screening. (A) Forster Radius (R_0) cut off for probe selection. From the total list of possible MuSIC probes (987), only probes with an R_0 value greater than 5nm (910) are selected as potentially good probes. (B) Potential number of MuSIC probes and barcodes. Given 18 fluorescent proteins, 910 MuSIC probes can be created (with an R_0>5nm), and given 910 MuSIC probes, 413,595 MuSIC barcodes could be created. (C) Example emission spectra of MuSIC probes and barcodes when excited at 405, 488, and 635nm. Given the fluorescent proteins mAmetrine and mOrange2, three MuSIC probes can be created that are spectrally unique. Given these three MuSIC probes, three MuSIC barcodes can be created. (D) Schematic showing the creation of MuSIC probes and barcodes from single fluorescent proteins. (E) Genetic and genetic interaction screening capabilities given the number of MuSIC probes that can be created.

Figure 2: Simulation setup. (A) Simulating emission spectra. Process of condensing the original emission spectra at every nm according to the emission binning and noise of the simulated instrument. (B) Cases for the simulation experiment setup based on Cytek flow cytometers.

Figure 3: Workflow for probe removal. (A) Obtaining the list of good probes based on classification metrics. First, the emission spectra of a mixture of probes is simulated given a set of probes. Next, noise is added to the emission spectra and the spectra is unmixed (using the reference matrix) to predict the mixture composition of probes. Binary classification is performed and finally, the predicted mixture composition is compared to the actual mixture composition. This process is repeated for each probe and the worst performing probe is removed until the overall classification is perfect. (B) Graphical representation of probe removal results. Individual probes are removed until the overall MCC value (confusion matrices shown on the right-hand side) is perfect (i.e equal to 1). (C) Workflow of sequential trimming of lists of good MuSIC probes. The final list of good MuSIC probes for single MuSIC probes (simulation 1) is used as the starting list for simulation 2. Then the final list of good MuSIC probes for barcodes (simulation 2) is used as the starting list for simulation 3.

Table 1: Simulated number of gRNA that could be used for genetic and genetic interaction screens. Results for the number of good probes that can be used to form barcodes and pairs of barcodes are shown for each experimental setup (the flow cytometer used), the number of lasers used, and the noise level (either low or high). Given the number of good probes, the number of potential gRNA for genetic and genetic interaction screens is listed. Results for the Cytek Northern Lights flow cytometer are highlighted in blue and results for the Aurora flow cytometer are highlighted in yellow.

Supplementary Figure and Table Legends

Figure S1: Comparison of lists of good probes between trials. The similarities and differences between the final lists of good probes for each trial are shown for each of the experimental setups.

Table S1: Fluorescent protein data. The maximum excitation and emission wavelength, brightness, extinction coefficient, and quantum yield for each fluorescent protein is found in the Attributes tab. Excitation and emission spectra for each fluorescent protein are found in the Excitation Spectra and Emission Spectra tabs, respectively. Sources for the raw data are found in the Sources tab.

Table S2: Probe lists. The lists of good probes for single probes, barcodes, and two barcodes are listed for each experimental setup in replicate.

Table S3:
Simulated number of gRNA that could be used for genetic and genetic interaction screens with variable probe expression levels. We allowed probe expression levels to vary between 0.5 and 1.5 (relative) to capture single cell-to-cell variability. Results for the number of good probes that can be used to form barcodes and pairs of barcodes are shown for each experimental setup (the flow cytometer used), the number of lasers used, and the noise level (either low or high). Given the number of good probes, the number of potential gRNA for genetic and genetic interaction screens is listed.

Table S4:
Simulated number of gRNA that could be used for genetic and genetic interaction screens when only considering one and two-way fluorescent protein probes. Probes containing three fluorescent proteins were not considered here. Results for the number of good probes that can be used to form barcodes and pairs of barcodes are shown for each experimental setup (the flow cytometer used), the number of lasers used, and the noise level (either low or high). Given the number of good probes, the number of potential gRNA for genetic and genetic interaction screens is listed.

Figure 1, McCarthy et al.

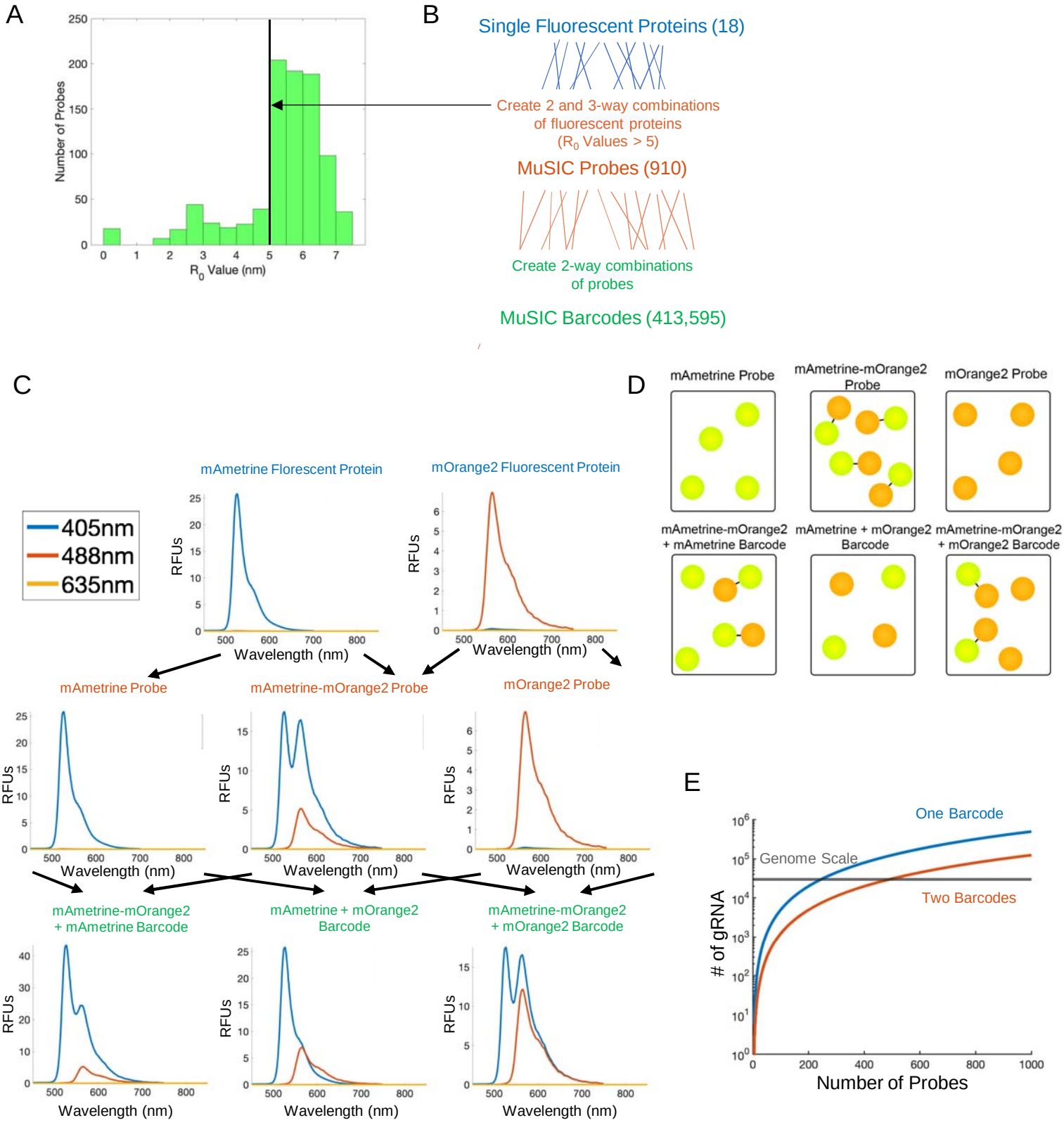

Figure 2, McCarthy et al.

A

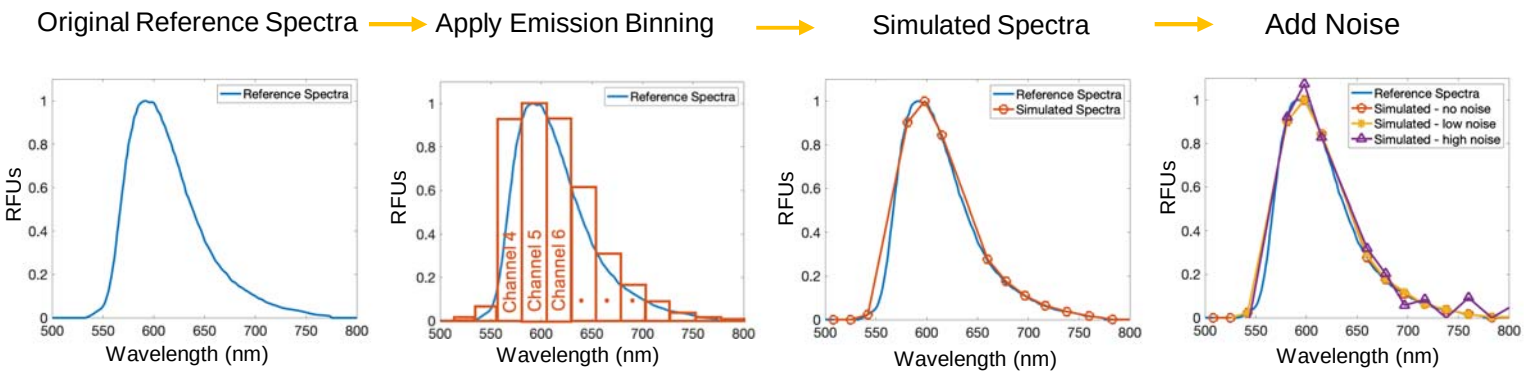

B

Simulation Stratification

Northern Lights - 3 Lasers
(405nm, 488nm, 635nm)

- 3 Lasers for demultiplexing
- 2 Lasers for demultiplexing
  1 Laser (635nm) for phenotype

Aurora - 5 Lasers
(356nm, 405nm, 488nm, 561nm, 635nm)

- 5 Lasers for demultiplexing
- 4 Lasers for demultiplexing
  1 Laser (635nm) for phenotype

Figure 3, McCarthy et al.

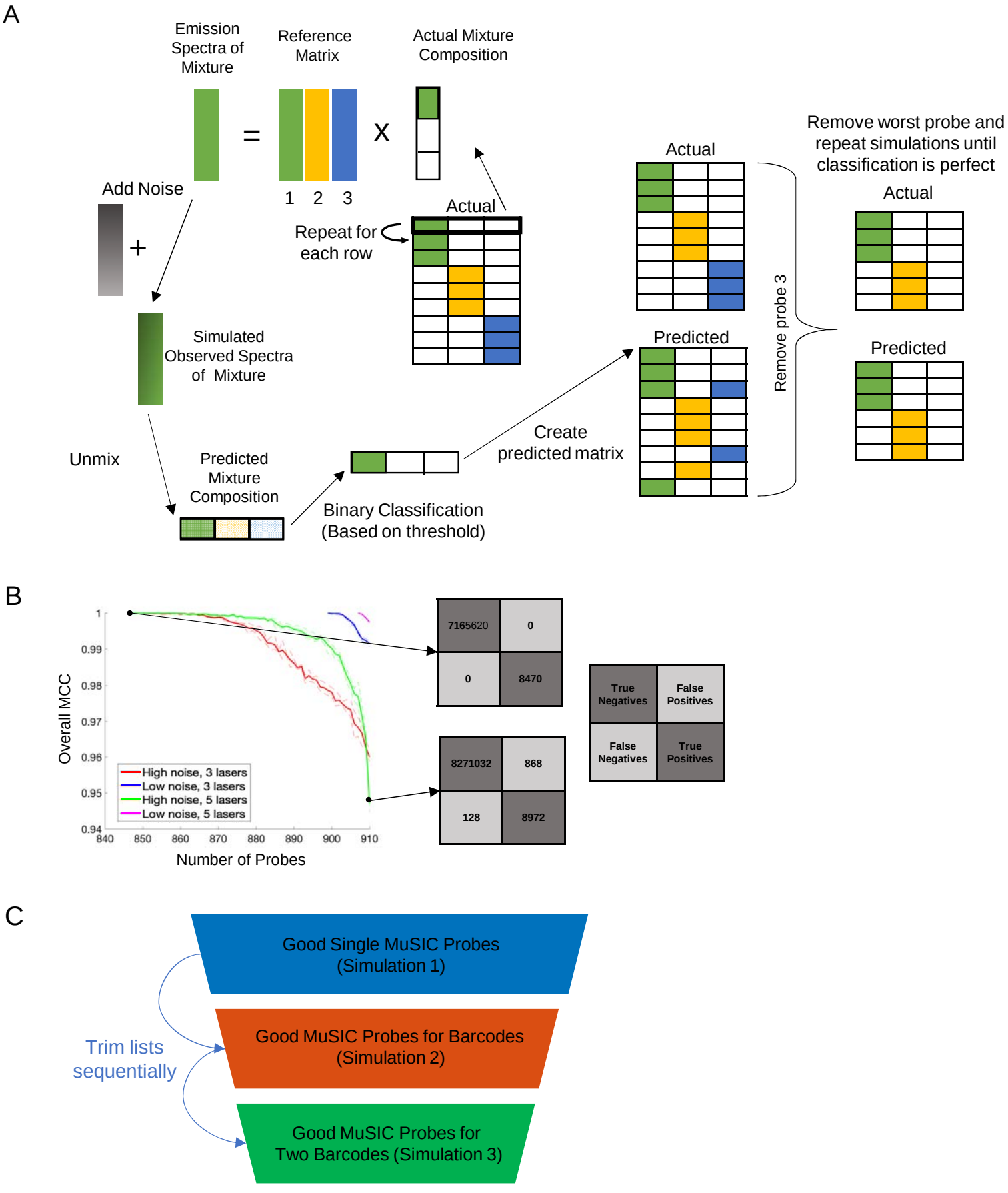

Table 1, McCarthy et al.

			# of Good Probes		# of gRNA	
Experimental Setup	# Laser	Noise	One Barcode	Two Barcodes	Genetic Screen	Genetic Interaction Screen
Cytek Northern Lights	3	high	337±3	113±5	56737±1001	1565±146
	3	low	634±5	230±11	200897±3149	6544±610
	2	high	292±8	92±5	42458±2445	1024±101
	2	low	550±25	175±12	151970±14008	3805±528
Cytek Aurora	5	high	666±15	294±7	221893±10020	10694±510
	5	low	894±3	708±12	399477±2596	62397±2046
	4	high	580±9	252±10	167983±4916	7860±654
	4	low	879±2	590±11	385885±1755	43294±1535

Supplementary Figure 1, McCarthy et al.

Single Probes

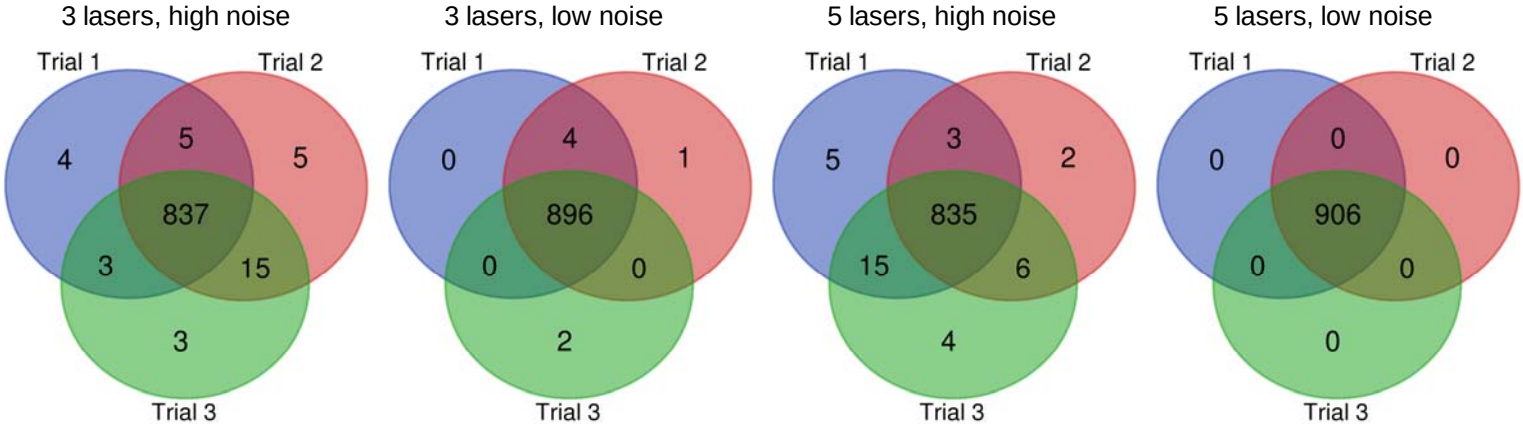

Barcodes

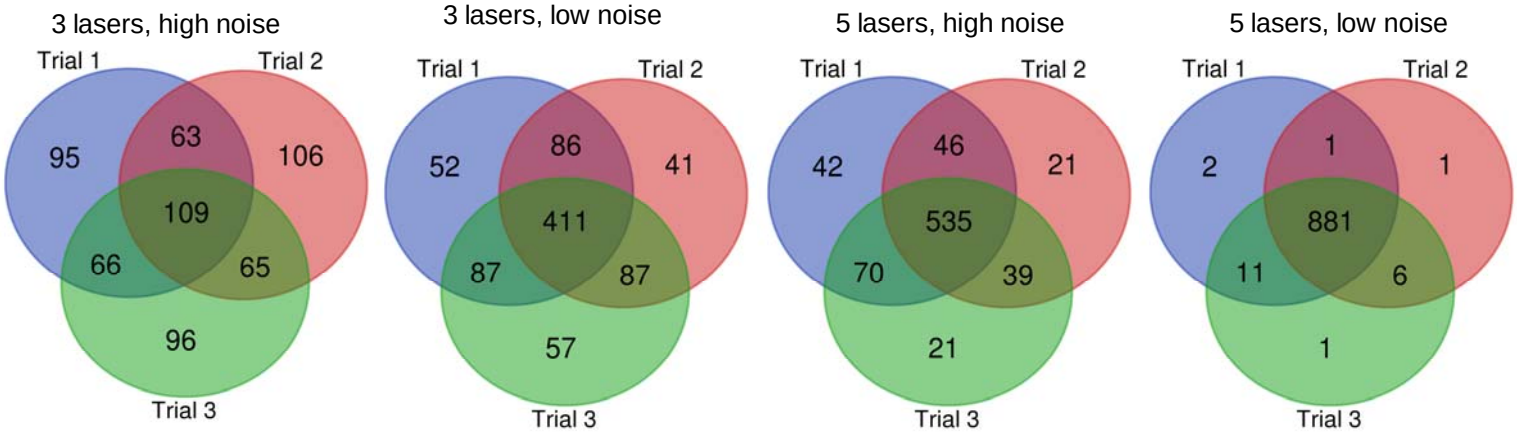

Two Barcodes

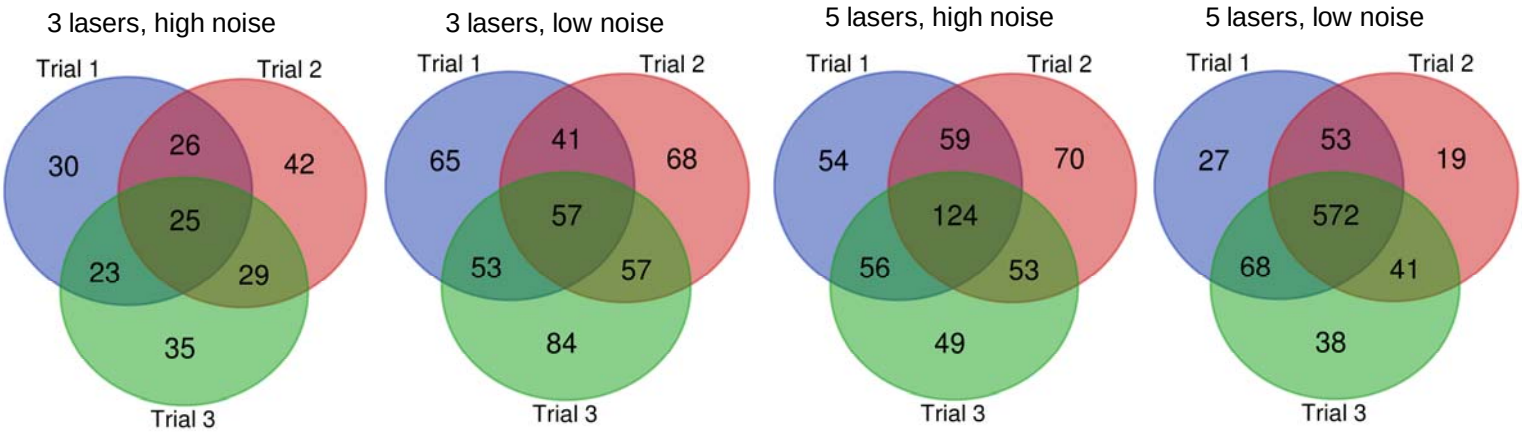

Supplementary Table 3, McCarthy et al.

			# of Good Probes		# of gRNA	
Experimental Setup	# Laser	Noise	One Barcode	Two Barcodes	Genetic Screen	Genetic Interaction Screen
Cytek Northern Lights	3	high	339±16	119±7	57440±5403	1741±189
	3	low	630±7	220±9	198184±4382	6014±474
	2	high	264±5	87±4	34831±1371	922±91
	2	low	538±16	164±6	144718±8708	3330±245
Cytek Aurora	5	high	619±15	299±2	191711±9555	11127±180
	5	low	888±3	689±13	393539±2309	59156±2306
	4	high	518±16	205±7	134331±8234	5198±367
	4	low	870±6	537±10	377763±5355	35803±1334

Supplementary Table 4, McCarthy et al.

			# of Good Probes		# of gRNA	
Experimental Setup	# Laser	Noise	One Barcode	Two Barcodes	Genetic Screen	Genetic Interaction Screen
Cytek Northern Lights	3	high	100±3	61±5	1211±71	451±74
	3	low	113±1	90=4	1559±10	979±80
	2	high	88±1	50±3	932±38	302±38
	2	low	109±2	69±2	1450±48	573±22
Cytek Aurora	5	high	104±2	91±2	1310±45	1006±53
	5	low	113±0	109±1	1559±19	1449±36
	4	high	102±2	81±2	1259±34	781±39
	4	low	114±0	109±1	1596±0	1431±31